Title

Impacts of Pore Network-Scale Wettability Heterogeneity on Immiscible Fluid Displacement: A Micromodel Study

Journal

Water Resources Research, 57(9)

ISSN

0043-1397

Authors

Chang, Chun
Kneafsey, Timothy J
Tokunaga, Tetsu K
et al.

Publication Date

2021-09-01

DOI

10.1029/2021wr030302

Peer reviewed

Impacts of Pore Network-Scale Wettability Heterogeneity on Immiscible Fluid Displacement: A Micromodel Study

Chun Chang*, Timothy J. Kneafsey, Tetsu K. Tokunaga, Jiamin Wan, Seiji Nakagawa

Energy Geosciences Division, Lawrence Berkeley National Laboratory, Berkeley, CA 94720, USA.

*Corresponding author. *E-mail address*: chunchang@lbl.gov

Key points

1. Fingering flow of hexane-ethylene glycol was investigated in mixed-wet micromodels with bimodal contact angle distributions at 47° and 145°.
2. Mixed-wettability diminishes displacement efficiency when contact angles vary beyond 90°, and at low capillary numbers.
3. We proposed a new set of capillary numbers to characterize the displacement and fingering flow in strong mixed-wet systems.

Abstract: The mixed-wet nature of reservoir formations imposes a wide range of rock wettability from strong resident-fluid wetting to strong invading-fluid wetting. The characteristics of two-phase flow in porous media composed of mixed-wetting surfaces remain poorly understood. In this study, we investigated the displacement of resident ethylene glycol (EG) by hexane in two mixed-wet micromodels of identical 2.5-D geometry heterogeneity, with uniformly or heterogeneously distributed patches strongly wetting to hexane. These patches are mixed among pores with unaltered EG-wetting surfaces. Along with control tests in the originally EG-wet micromodel, we show the classic fingering and transitions in flow regimes at $logCa$ (capillary number) from −7.2 to −3.9. Moreover, pore-scale distributions of wettability and their spatial correlation influence displacement efficiency. In the two mixed-wet micromodels, we found (1) an increase of steady-state hexane saturation at the end of experiments by up to 0.12 in the capillary fingering regime and a decrease of at most by 0.06 in the viscous fingering regime, compared to the EG-wet micromodel, and (2) dispersed and fragmented hexane distribution after displacement. Brine drainage during supercritical CO_2 ($scCO_2$) injections in these micromodels occurs with lower wettability contrasts, and under similar viscosity ratios and interfacial tensions resulted in higher displacement efficiency relative to displacement of EG by hexane. While mixed-wettability can enhance displacement efficiency compared to uniform wettability, the dynamics of immiscible fluids in strong mixed-wet reservoirs are expected to be less pronounced in contributing to the efficiency of geological CO_2 sequestration, oil recovery, and remediation of hydrocarbon-contaminated aquifers.

1. Introduction

Two-phase flow in the subsurface involves unstable displacement and fingering flow when a viscous resident fluid is displaced by an invading fluid of lower viscosity (Saffman & Taylor, 1958; Nittmann et al., 1985). The related reservoir practices include geological CO_2 sequestration (GCS), hydrocarbon (oil) resources recovery and non-aqueous phase liquid (NAPL) contamination/remediation of groundwater (Zhang et al., 2011; Wang et al., 2012; Nicolaides et al., 2015). The unstable displacement can be further complicated by rock surface wettability, as the slow subsurface flow and fingering is dominated by capillary forces (Kuo and Benson, 2015; Chang et al., 2020). While most sandstone reservoirs present strong water-wet surfaces, a large majority of carbonate reservoirs tested are oil wet (Anderson, 1986). The original strong water wetting nature of most reservoir minerals can also be altered by the adsorption of organic matter that was originally in the crude oil (Morrow et al., 1986; Jadhunandan and Morrow, 1995). The degree to which the wettability is altered is determined by pressure, temperature, mineral surface, and brine chemistry, including ionic composition and pH (Gribanova et al., 1976; Hirasaki, 1991, Iglauer, 2017). The spatial distribution characteristics of the altered rock surface are affected by the flow of crude oil and other active agents (e.g., CO_2 during GCS). All these complexities can result in mixed-wet reservoir rock, presenting a full spectrum of solid surface wettability from strong water wetting to strong oil wetting (Salathiel, 1973). In this case, both drainage and imbibition could occur, where (1) drainage refers to the displacement of a resident fluid wetting to rock surfaces by a less wetting invading fluid, and (2) imbibition is defined as the displacement of a resident fluid by an invading fluid more wetting to the rock surfaces.

Extensive laboratory and modeling studies have been conducted to investigate fingering flow fundamentals, including displacement efficiency and distribution characteristics under drainage (Lenormand 1988; Ferer et al., 2004; Kang et al., 2004; Chang et al., 2019a) and imbibition (Hughes and Blunt, 2000; Nguyen et al., 2006; Armstrong et al., 2014; Castro et al., 2015; Chang et al., 2019b). Significant attempts have also been made to understand the impacts of solid surface wettability from pore to reservoir scale (Al-Khdheeawi et al., 2017; Anderson, 1987a,b; Morrow, 1990; Levine et al., 2014; Cottin et al., 2011; Zhao et al., 2016; Hu et al., 2017a,b). At the pore scale, transition of fingering flow characteristics has been reported by Zhao et al. (2016) in micromodels of identical geometry, but varying – yet uniform – surface wettability inducing strong drainage to strong imbibition. Chang et al. (2020) created two mixed-wet systems of different water-wet and intermediate-wet patches in a 2.5-D heterogeneous micromodel. Along with the originally water-wet micromodel, the impacts of mixed-wettability on brine drainage and supercritical CO_2 ($scCO_2$) storage efficiency were investigated by injecting $scCO_2$ into the initially brine-saturated micromodels at a wide range of flow rates. While their results indicate the importance of mixed-wettability in determining CO_2 saturation and distribution characteristics at GCS conditions, the *'weak'* mixed-wet systems composed of water-wet and intermediate-wet patches result in dominant drainage of brine under high and low capillary numbers. However, in a *'strong'* mixed-wet system where contact angles of immiscible fluids on solid surfaces vary beyond 90° (Kumar et al., 2012; Alhamadi et al., 2017), the two-phase flow characteristics and displacement efficiency remain poorly understood and need systematic study.

In two-dimensional (2-D) systems, the classic capillary number (Ca), in its original form: $Ca = \mu \times \bar{u} / \sigma$, was used to interpret the fingering geometry in a Hele-Shaw cell by Saffman & Taylor (1958). In this definition of Ca, $\mu$is the viscosity of the resident fluid, $\bar{u}$ is the average Darcy velocity of the injected fluid, and σ is the interfacial tension between the injected and resident fluid. Given negligible influences of gravitational forces in thin micromodels, the classic Ca, along with the mobility ratio (*M*) defined as the ratio of viscosities of the displacing (non-wetting) and displaced (wetting) fluids, were used to characterize the pore-scale regimes of stable displacement, capillary fingering, viscous fingering, and the crossover between them. After Lenormand (1998) and considering the effective contact angle between two fluids on solids that present a uniform wetting surface, the modified $Ca^{¿}$¿¿) has been widely adopted to quantify (1) the fingering flow regimes and transition from capillary fingering to viscous fingering during drainage (Xu et al., 1998; Ferer et al., 2004; Cottin et al., 2010; Zhang et al., 2011; Wang et al., 2012; Armstrong & Berg, 2013; Chang et al., 2019a), and (2) the capillary desaturation and imbibition flow regimes (Sahimi, 1993; Hilfer & Oren, 1996; Armstrong et al., 2014; Castro et al., 2015, Chang et al., 2019b). Note there are very different flow fundamentals and distribution characteristics between drainage and imbibition. When drainage occurs, pores with wetting fluid can drain and be filled with non-wetting fluid when the local capillary pressure is higher than the threshold entry pressure, thus the largest pores typically get drained first. During imbibition, smaller pores tend to fill first with the wetting phase (invading fluid) by corner and film flow, but the wetting phase may never imbibe into all pores of a given size as a result of entrapment of the non-wetting phase by snap-off (Roof, 1970; Dong & Chatzis, 1995; Valvatne & Blunt, 2004; Tokunaga, 2009; Cihan et al., 2014). A single Ca arbitrarily considering the acute angle (regardless of measuring on the resident or invading fluid) is clearly insufficient for quantifying drainage and imbibition, two-phase distribution, and displacement efficiency in a mixed-wet porous media contains strong contrasts in surface wettability.

In this study, a series of experiments were conducted by injecting hexane into an initially ethylene glycol (EG) saturated micromodel at different displacement rates which resulted in $logCa$ (logarithm of the capillary number) ranging from −7.2 to −3.9. On the basis of similar viscosity ratio and interfacial tensions (IFT), these experiments were used to compare with $scCO_2$-water drainage in the same micromodel from Chang et al. (2020), and investigate the impacts of pore networks composed of mixed-wet patches strongly wetting to either resident or displacing fluids. For simplicity and ease of comparisons with other studies, the first form of the capillary number Ca used in this presentation does not include a contact angle term. We further (1) quantify the distribution characteristics for both fluid pairs at the pore- and pore-network scale through a topological analysis, and (2) propose a new $dCa^{¿}-iCa^{¿}$ diagram to characterize the drainage and imbibition flow in the two mixed-wet micromodels. Here, drainage (d) and imbibition (i) refer to displacement of the native fluid from pores that are wetting and non-wetting with respect to the invading fluid, respectively. During the experiments, images of hexane and EG distribution were obtained to provide direct observations on the pore- and pore-network scale displacement characteristics, and compared with $scCO_2$-brine in the identical pore geometry and mixed-wet patterns, but different contact angles and wettability contrasts.

2. Materials and methods

2.1 Micromodel

The micromodel used in this study is a depth variable pore network, with a porosity of 0.43 and pore volume of 3.44 µL in a 20 mm ×10 mm rectangle. The pore configuration shown in Figure 1(a) was extracted from micro-CT images of sand pack of irregular shaped sand grains, etched on two symmetrical silica wafers with hydrofluoric acid and then fused together (Micronit Microfluidics BV, Netherlands). The different depths of pores and pore throats were created through etching two mirror image networks, both to 20 µm depths, but with one face having pore locations left unetched. In each silica wafer, acid dissolved the wafer under a mask equally in all directions. This made the etched channels grow in all directions, resulting in round corners and a slightly smaller bottom channel width compared to the top channel width. Thus, 40 µm deep pores (marked in white) are created at locations where both faces were etched to 20 µm, while 20 µm deep throats (marked in red) were created at locations where only one face was etched. The pore and pore-throat size at 40 µm deep is 190± 88 µm, determined by a local thickness plugin in ImageJ software (Hildebrand and Rüesgsegger, 1996; Rasband, 1997–2021). The 20 µm deep pore throats account for 3% of the pore space in the pore network, at an average size of 48± 17 µm. We thus do not expect considerable errors using 2D images in interpreting two-phase flow and distribution in the 2.5-D micromodel. The post (grain) size is measured as 290± 91 µm. The pore network is also characterized by a capillary barrier transverse to the flow direction, composed by a line of tight pore throats 20 µm deep (see the magnified image of Figure 1(b)). There are eight full depth

(40 μm) pores along the capillary barrier, with all the others being only 20 μm deep. These eight "slots" constitute pores with low capillary entry pressures and impact invasion of hexane, which will be shown in Section 3.2. More details of the micromodel can be found in Chang et al. (2020).

2.2 Experimental procedures

2.2.1 Mixed-wet treatment and contact angle quantifications

Two syringe pumps (Harvard Apparatus, MA) were used at ambient conditions for both mixed-wet treatments and hexane-EG displacement experiments in the micromodels having the same pore geometry. To better observe the two-phase interface, we colored the EG with sulphorhodamine B and collected images of dyed EG distribution under UV light. A low dye concentration (0.23 g/L) was used to minimize its potential effect on fluid viscosity, while allowing sufficient optical detection for phase discrimination. A Sony FDR-AX100 4K camcorder was installed over the micromodel to record images at a spatial resolution of 4.5 μm/pixel.

The wettability-altering solution was prepared by diluting octadecyltrichlorosilane (OTS) (Cole-Parmer, IL) with hexane (ACS grade, Cole-Parmer, IL) in 0.2% volumetric fractions. During the wettability treatment, the micromodel was first acetone cleaned, air dried and then saturated with dyed EG. The surface coating OTS solution was then injected at constant flow rates using a syringe pump. Over 3 and 300 pore volumes (PVs) of coating solution were injected into the two micromodels at $logCa$=–7.2 (3 μL/hour) or $logCa$=–3.9 (6000 μL/hour), respectively, until the two-phase distribution in the pore network remained constant with time (see Figures 1(c) and (d)). Other mixed-wet patterns may vary between these rates, but these two limiting cases are worth detailed investigation. The coating solution injection ceased after it was allowed to reside for over 20 min in the pore network, followed by 100 PVs of hexane injection to remove excess OTS solution from the pore network. Finally, the micromodel was air-dried and cured in an oven at 100 °C for 1 hour. Contact angle measurements of dyed EG droplets on clean glass microscope slides surrounded by hexane showed values change from 46° (strong EG wet) to 140° (strong hexane wet) after treatment, even after 2 years, indicating the long-term effectiveness of the method (Figure S1 of the supporting information (SI)). More details on the mixed-wettability treatment of micromodel and microscope slides can also be found in Chang et al. (2020).

Figure 1. (a) Pore characteristics of the 2.5-D micromodel used in this study, with solid posts shown in black, large pores 40 μm deep shown in white and tight pore throats 20 μm deep in red. (b) The sub-image magnified from the red box in (a) that shows the transverse capillary barrier in the pore network. The quasi-steady state distribution of dyed EG (red color) in the two micromodels after OTS injection from the left side at (c) $logCa$=–7.2, and (d) $logCa$=–3.9. (c) and (d) thus represent mixed-wet patterns induced by capillary and viscous fingering, respectively. The red arrows in (b) mark the open slots in the capillary barrier with 40 μm deep pores that may provide potential flow paths for hexane invasion. The blue boxes in (a) and (b) bound the local pore domain that correlates to the narrow hexane-wet choke point in (c) (marked by the white arrow) and constrained hexane flow in Figure 3(b). The white dotted curve in (c), as an example, marks an individual EG cluster, while the blue arrow in (a) indicates the flow direction of the coating solution during treatment. Rearranged and modified from Chang et al. (2020).

Contact angles were also measured for hexane-EG in-situ of the micromodel under ambient conditions. Both of the untreated and treated mixed-wet micromodel were initially EG-saturated, followed by hexane injection at a low rate until the hexane-EG distribution in the micromodel was stable with time. Images of stained EG were taken to measure hexane-EG contact angles on solid posts. Menisci of hexane-EG interface were selected such that each meniscus possessed a flat contact line of sufficient length so that the change in post geometry and surface roughness did not considerably affect the contact angle measurements. The menisci were selected randomly over the entire pore network.

2.2.2 Displacement experiments

Following wettability treatment in each of the two mixed-wet systems, hexane was injected into the initially EG-saturated micromodel at a specific constant flow rate. Displaced EG was collected through capillary tubing at ambient conditions. When the quasi-steady state was reached, i.e., hexane distribution and saturation remained constant with time, hexane injection was stopped. The micromodel was then flooded with EG at a high flow rate until no hexane was observed in the pore network, in preparation for the next experiment conducted at a different hexane injection rate. This sequence was repeated for ten hexane injection tests at a wide range of flow rates from $logCa = -7.2$ to –3.9. These capillary number values are representative to CO_2 flow at 0.01 to 14 m away from a typical injection well (with an injection rate of one million metric tonnes of CO_2 per year over a screen length of 15 m assuming uniform flow) at a GCS site.

The viscosities of hexane and dyed EG were assumed equal to that of hexane (0.3 mPa·s) and EG (16.9 mPa·s) due to the low dye concentration, while the IFT between hexane and dyed EG at ambient conditions was measured as 20.5 mN/m with a high-precision tensiometer (Kruss, Germany). Note the similar viscosity ratios and IFTs between hexane-EG under ambient conditions and $scCO_2$-water system at 8.5 MPa and 45 °C ($\mu_{CO2} =$ ¿ 0.023 mPa·s, $\mu_{brine} =$ ¿ 0.6 mPa·s, IFT: 28.5 mN/m) in Chang et al. (2020). With these similarities, the impacts of the mixed-wet patterns and wettability contrasts on flow characteristics of hexane-EG vs. $scCO_2$-brine can be investigated and compared.

2.3 Image analysis

Segmentation and analysis of the images were conducted using ImageJ - public domain JAVA based software (Rasband, 1997–2021). The raw images taken during a displacement test were first subtracted from the image taken at the initially EG-saturated condition, followed by a median filtering of the resulting images. A threshold value was then unambiguously determined for each image to distinguish hexane phase from others. Figure S2 of SI presents an example image of the local pore domain (3.8 × 3.7 mm^2) selected to illustrate the EG phase segmentation. The accuracy of hexane phase segmentation was verified by comparing the area in the binary image (Figure S2(b)) vs. the pore space area filled by hexane in the subtracted domain (Figure S2(a) of SI). Results showed an error of 0.5% from the binary segmentation, mostly originated from the edges and connectivities in the narrow pore throats. The resulting binary images were then used to present the flow characteristics and calculate hexane saturation in the EG-wet and two mixed-wet micromodels.

3. Results and discussion

In this section, we first present the contact angles measured for hexane-EG before and after coating treatment in Section 3.1, followed by hexane saturation and distribution at injection rates varying from $logCa$ = –7.2 to –3.9 in the EG-wet and two mixed-wet 2.5-D micromodels in Sections 3.2. In Section 3.3, we compare the results with $scCO_2$-water through a topological analysis at the pore- and pore-network scales, and investigate the impacts of pore-networks composed of mixed-wet patches strongly wetting to either of the resident or displacing fluids. We then propose a new $dCa^{¿}-iCa^{¿}$ diagram to characterize the drainage and imbibition in the two types of mixed-wet micromodels in Section 3.4, followed by discussion on field and modeling implications of the laboratory results.

3.1 Contact angle and mixed-wet patterns for hexane-EG

Figure 2(a) presents an example image of the local pore domain showing the variability of contact angles between hexane (purple) and EG (yellow to white) in the treated micromodel shown in Figure 1(d). Within the local pore domain of 3.9×3.0 mm^2, the contact angle varies considerably from 41° to 145°, while bimodally distributed depending on whether the injected coating solution has contacts with the post surfaces. Figure 2(b) further compares the contact angles obtained from over 60 menisci selected within the entire pore network. In the untreated micromodel, the average contact angle is measured as 46.7±2.6°, showing a strong EG-wet surface and similar to the measurements on glass slides. Figure 2(b) also shows considerable increase of the contact angle to an average value of 145±4.1° after OTS treatment, changing the pore surface from strong EG-wet to strong hexane-wet. Note that we measured the contact angle of menisci over the entire pore network where both hexane and brine were present. By Figure 2(b), we may infer that the wettability of pore space invaded by coating solution during treatment was altered to non-wetting, and that saturated with EG retained its original water-wet surfaces. We do not expect considerable wettability changes of the treated micromodels after the displacement experiments by comparing the contact angles in the same pore domain shown in Figure 2(a) before and after tests (see Figure S3 in the SI). In a previous study, Alhammadi et al. (2017) used X-ray micro-tomography to directly image the distribution of contact angles in calcite cores from a producing hydrocarbon reservoir at subsurface conditions. Their results show the large varieties of contact angles from 48° to 140°, representing strong mixed-wet rock surfaces similar to the treated micromodels. In Section 3.2, we examine the invasion of hexane through the mixed-wet micromodels, and displacement of resident EG from the EG-wetting pores (drainage) and from the hexane-wetting pores (imbibition).

Figure 2. (a) An example image showing the wide range of contact angles between hexane (purple) and EG (yellow to white) in a local pore domain after OTS treatment (grain posts are shown in black). (b) The contact angle measurements from 60 selected menisci within the pore network for both untreated and treated micromodels. The dotted lines in (b) represent the average contact angles for the untreated (black color) and treated (red color) post surfaces at 46.7 ± 2.6° and 145 ± 4.1°, respectively.

To better quantify the mixed-wet patterns and differences between the two mixed-wet systems, we define a EG cluster composed of multiple pores/pore throats filled with EG, while the boundary of each cluster is surrounded by the invading OTS solution and/or grain posts (e.g., one bounded by the white dotted line in Figure 1(c)). We measured area and maximum length of each EG cluster, then the area-weighted cluster length was obtained as 2560 ± 1870 μm for the mixed-wet pattern induced by capillary fingering in Figure 1(c). The average cluster length was similarly measured as 870 ± 596 μm in Figure 1(d) for the mixed-wet pattern induced by viscous fingering. The number of clusters (defined as cluster number hereafter) is 325 in the former vs. 967 in the latter. These indicate that the EG-wet and hexane-wet pores are more heterogeneously distributed in Figure 1(c), and more well-mixed and uniformly distributed in Figure 1(d). We thus refer to (1) the micromodel where the hexane-wet pores were capillary-force induced and heterogeneously distributed in the pore network as the heterogeneous mixed-wet (HM) micromodel; and (2) the micromodel where the hexane-wet pores were viscous-force induced and more uniformly distributed in the pore network as the uniform mixed-wet (UM) micromodel.

3.2 Fingering flow and hexane saturation

3.2.1 Displacement in the 2.5-D EG-wet (EW) micromodel

Figure 3(a) shows the quasi-steady state hexane distributions after displacements in the untreated EW micromodel. The numbers in the parentheses are corresponding displacement rates ($logCa$) and hexane saturations. The hexane distributions indicate the classic fingering regimes and transition with injection rates. For instance, capillary fingering dominates at low displacement rate ($logCa<-6.2$), where hexane flows in forward and lateral flow paths with large entrapped EG clusters; viscous fingering develops at large displacement rate ($logCa> -6.2$), where hexane widely invades the pore network and displaces resident EG in the form of multiple narrow and well-connected flow paths. At the intermediate rates ($logCa=-6.2$), crossover from capillary to viscous fingering is shown by the coexistence of distributed capillary fingering (near the upstream) and concentrated viscous fingering (near the downstream), resulting in pronounced hexane saturation reduction to 0.43. Figure 3(a) also presents the considerable impacts of the 2.5-D heterogeneity in pore geometry. We observed the hexane passed easily through the open slots (marked by the white circles) of the transverse barrier that were close to the top and bottom boundaries, and bypassed the barrier and even some slots in center (marked by the red circles). The half-depth barrier hindered longitudinal hexane flow in the center and enhanced transverse flow that bypasses the slots ahead. At $logCa \geq -4.6$, hexane invaded most of the slots under the strong viscous force. A local pore domain was selected (marked by the red frame in Figure 3(a)) to better understand the pore-scale flow characteristics and compare with $scCO_2$-brine in Section 3.3.2. The overall hexane flow regimes and transitions with imposed $logCa$ are similar to Lenormand et al. (1988), Wang et al. (2012) and Ferer et al. (2004). Furthermore, the $logCa$ value corresponding to minimum hexane saturation (−6.2) is similar to $scCO_2$-brine displacement at −6.4 from Chang et al. (2020).

3.2.2 Displacement in the 2.5-D mixed-wet micromodels

Figures 3(b) and (c) present the hexane flow and saturation in the two mixed-wet micromodels, where 50% of pore space in the HM and 70% in the UM micromodel were changed to strongly hexane wetting (θ =145°), with remaining pore space sustained strongly EG wetting (θ=47°). The classic flow regime transition from capillary fingering through crossover to viscous fingering can also be observed, however, the $\log Ca$ value corresponding to the minimum hexane saturation increases from −6.2 in the EW to −5.6 in the two mixed-wet systems. Compared to the uniform EW micromodel, hexane saturations are higher in the two mixed-wet micromodels in the capillary fingering regime ($-7.2 \leq logCa \leq -6.2$), while slightly lower in the viscous fingering regime ($-5.2 \leq logCa \leq -3.9$).

We also show in Figure 3 the pronounced impacts of mixed-wettability on hexane distribution. For instance, in the HM micromodel and at the intermediate-rate injection ($\log Ca$ = −5.6), we observed a single hexane flow path developed at the barrier downstream (marked by the white arrows in Figure 3(b)). This single flow path gradually developed into several dendritic paths towards the outlet. The unique hexane flow pattern can be attributed to the preferential flow through the narrow hexane-wet (instead of geometrically induced) choke point marked by the white arrow, similar to the $scCO_2$ flow pattern in the same HM micromodel from Chang et al. (2020). Lower and higher injection rates resulted in additional flow paths around it.

Figure 3. The quasi-steady state hexane (shown in green) distribution after displacement in the micromodel of (a) EG-wet (EW), (b) heterogeneous mixed-wet (HM) and (c) uniform mixed-wet (UM). The numbers in the parentheses are $logCa$ values and steady-state hexane saturations at the end of experiments, respectively. Hexane is injected at the left side of these images, as indicated by the blue arrow. The circles refer to the open slots in Figure 1(b) invaded (white) and bypassed (red) by hexane. The white arrows in (b) indicate the constrained hexane flow induced by the narrow hexane-wet choke point. The red frames in (a), (b) and (c) mark the local pore domains selected for analyzing pore-scale flow characteristics and mixed-wettability effects in Figure 5.

3.3 Comparisons with CO_2-brine displacement

In this section, we show more detailed analysis of the hexane-EG flow characteristics at the pore and pore-network scale, and compare these with $scCO_2$-brine displacement at

8.5 MPa and 45 °C. For $scCO_2$-brine, the same mixed-wet micromodels show relatively small wettability and contact angle contrasts (27° measured for untreated water-wet vs. 89° for treated intermediate-wet surfaces), thus drainage of brine is the dominant process. For hexane-EG, the more pronounced wettability contrasts between patches of EG-wet (contact angle at 47°) vs. hexane-wet (contact angle at 145°) may results in co-occurring (1) drainage of EG in strong EG-wet patches, where hexane invades large pores/pore throats, displaces resident EG and develops connected flow paths, and (2) imbibition of hexane in strong hexane-wet patches, where hexane invades small pores/pore throats via film and corner flow, along with residual trapping of EG ganglions by snap-off and fragmented hexane flow paths. These impacts on the displacement efficiency are discussed in Section 3.3.1. The impacts on phase distribution characteristics are further quantified and compared by a topological analysis applied to (1) a local pore domain at 3.8×3.7 mm^2 in vicinity of the capillary barrier (indicated by the red frames in Figure 3) in Section 3.3.2, and (2) the entire pore network for all the displacement tests in the three micromodels in Section 3.3.3.

3.3.1 Displacement efficiency

Figure 4 compares the steady-state hexane and $scCO_2$ saturations in the three types of micromodels at imposed $\log Ca$ values from −8.1 to −3.9. In the untreated EW/WW (water-wet) micromodel (Figure 4(a)), the quasi-steady state hexane and $scCO_2$ saturations are similar at ~0.50 under low imposed $\log Ca$ values (−7.1 and −7.2), when the fingering flow regime for both is dominated by capillary force. Increasing the $\log Ca$ results in (1) more pronounced CO_2 flow channelization thus lower saturation at flow regime crossover from capillary to viscous fingering (−6.8 $\leq \log Ca \leq$ −5.4), and (2) more compact invasion and higher CO_2 saturation at the viscous fingering regime ($\log Ca \geq$ −5.1). These represent more considerable variations in displacement efficiency for $scCO_2$-brine as a function of $\log Ca$ under the drainage-dominated flow.

In the HM micromodel, Figure 4(b) shows that hexane saturations are similar to $scCO_2$ saturations in the capillary fingering regime, but lower at the viscous fingering and flow regime crossover. In the UM micromodel, as shown by Figure 4(c), hexane saturations are lower than $scCO_2$ saturations at all the fingering flow regimes and crossover. Compared to $scCO_2$-brine displacement, the displacement efficiency of hexane is overall hindered in the mixed-wet micromodels at imposed $\log Ca$ values from −7.2 to −3.9. Also note that the $\log Ca$ values corresponding to the minimum $scCO_2$ saturation are constant at −6.4 in the three types of micromodels, but the $\log Ca$ values for hexane saturation minima increase from −6.2 in the EW to −5.6 in both of the mixed-wet systems. These indicate that a single Ca is insufficient for quantifying displacements in the two mixed-wet micromodels. We will propose and discuss a new $\log\left(d\,Ca^{¿}\right)-\log\left(i\,Ca^{¿}\right)$ diagram for better displacement quantification in Section 3.4.

Except for the positions of their saturation minima (thus the fingering flow crossover) changes due to mixed-wettability, variations of the steady-state hexane/$scCO_2$ saturations vs. $\log Ca$ exhibit similar ‘V’ shapes, following the classic regime transitions from capillary to viscous fingering (Figure 4). These ‘V’ shape variations reflect similar fingering flow fundamentals between hexane-EG and $scCO_2$-water systems, dominated by either capillary or viscous forces.

Figure 4. The steady-state saturations of hexane vs. $scCO_2$ at the end of experiments at imposed $\log Ca$ values in the (a) EW(WW), (b) HM and (c) UM micromodels, respectively.

3.3.2 Pore-scale distribution characteristics

We selected a local pore domain located by the red frames in Figure 3 to further investigate the drainage and imbibition flow at the pore scale. As shown in Figure 5(a), the pore domain is composed of (1) ~100 solid posts (shown in black), (2) large pores 40 μm deep (shown in yellow) and (3) tight pore throats 20 μm deep (shown in red). The average pore and pore-throat width is measured as 204 μm and 80 μm, respectively, while the porosity is 0.44, similar to the entire pore network. More detailed descriptions of the pore domain can be found in Chang et al. (2020). Figures 5(b) and (c) depict the OTS-altered patches (marked in white) in the HM and UM domains, accounting for 66% and 77% of the pore space, presenting strong hexane-wetting (145°) for hexane-EG and intermediate-wetting (89°) for $scCO_2$-brine. Figures 5(d), (e) and (f) show the hexane distributions (white color) in the three pore domains after displacement dominated by flow regimes that crossover from capillary to viscous fingering. The numbers in the parentheses indicate corresponding $\log Ca$ values and hexane saturations. As shown in Figure 5(d), hexane invades the pore domain from the top left corner, transversely flows through the domain along the red dotted arrows and flows out of the domain at the bottom center. Note the bulk flow direction is from left to right. Blockage of hexane by the EG-filled capillary barrier occurs, resulting in flow direction changes and bypass of tight (only 20 μm deep) pore throats. After injection, the hexane saturation in the EW domain is stable at 0.44. In Figures 5(e) and 5(f), the steady-state hexane saturations after displacement are similar at 0.46 and 0.47 in the HM and UM domain, among which 89% and 72% is distributed within the hexane-wet patches.

While hexane saturations are similar in the three wetting types of pore domains, mixed-wettability greatly changes the hexane distribution. Hexane in the two mixed-wet pore domains becomes more dispersed, with large EG clusters trapped and surrounded by thin hexane flow paths (see Figures 5(e), (f)), in contrast to concentrated hexane flow with large bypassed EG clusters in Figure 5(d). Figure 5(j) compares the hexane saturation vs. pore/pore throat size distribution in the three types of pore domains. The majority of hexane is distributed in large pores/pore throats > 80 μm wide and 40 μm deep, with less than 1% in the tight 20 μm deep pore throats. The colored dashed lines in the figure indicate that over 50% of hexane is distributed within pores/pore throats 70-205 μm in diameter in the EW domain, whereas same amount of hexane invades smaller pores/pore throats in the two mixed domains (e.g., 45-196 μm in the HM and 45-188 μm in the UM domains). For $scCO_2$-brine in Figure 5(k), the corresponding ranges change less, from 65-224 μm in the WW, to 65-226 and 60-208 μm in the HM and UM domains, respectively.

The distribution characteristics of hexane flow paths are further quantified in the same local pore domain using an Analyze Skeleton plugin in ImageJ. The skeleton geometry is defined as a thin version of that geometry which is equidistant to its boundaries. The binary images of hexane and $scCO_2$ in the three types of pore domains (Figures 5 (d), (e), (f) and (g), (h), (i)) are first skeletonized in ImageJ and illustrated by branches and junctions. Figure S4 in the SI presents an example of the skeletonized image with marked branch and junction. Specifically, a branch is composed of a group of pixels that have exactly 2 neighbor pixels, while a junction is defined as the intersection of multiple (more than two) branches, i.e., the junction pixels have more than 2 neighbors. The number of branch and junction, and the average branch length were first calculated for hexane flow paths ($N_{b,hexane}$, $N_{j,hexane}$ and L_{hexane}) and for the pore domain (N_b, N_j and L), then their ratios, defined as the specific branch number ($N_{b,hexane}/N_b$), specific junction number ($N_{j,hexane}/N_j$) and specific branch length (L_{hexane}/L) were calculated and presented in Table 1. Table 1 also lists the specific branch and junction number, and specific branch length for $scCO_2$. Similar to Section 3.1, we define a cluster of hexane/$scCO_2$ as pores/pore throats that are filled and connected by hexane/$scCO_2$, while each cluster is isolated by the residual EG/brine phase and/or grain posts (e.g., one marked by the blue line in Figure 5(d)). The number of clusters for both in each type of domain is listed as cluster number in Table 1.

For hexane, the cluster numbers increase monotonically from 3 in the EW to 10 in the HM, and to 16 in the UM domain, as more pore space was altered to hexane wetting. Accordingly, both of the specific branch and junction numbers increases and the specific branch length decreases in the mixed-wet domains. These changes indicate the increasingly dispersed flow and fragmented distribution of hexane in the HM and UM domains, due to (1) the film and corner flow of hexane that propagates along the small pores/pore throats and snap-off of non-wetting EG ganglions (marked by the red solid arrows in Figure 5 (f)) in the hexane-wet patches, and (2) the flow of EG ganglions along with displacing hexane behind the invasion front, over a length of tens of pores, and refill of the pore (pointed to by the blue arrow in Figure 5(f)) preferentially invaded by hexane (see more details in Figure S5 of SI). In a uniform wetting micromodel, Armstrong and Berg (2013) have reported that the pore drainage events and invasion of non-wetting fronts are cooperative, meaning that capillary pressure differences could extend over multiple pores and directly affect fluid topology and menisci dynamics. In a mixed-wet system, we show the migration of resident ganglions could also occur over multiple pores behind the displacement fronts and further fragment the invasion phase.

For scCO_2 in the WW domain, the cluster number is higher than hexane (the ratio is 1.33:1), resulting in a proportional increase of specific branch number (1.30:1) and specific junction number (1.35:1). Meanwhile, the specific branch length for both scCO_2 and hexane is close to 1.0, indicating similar topological characteristics of individual clusters dominated by pore geometry. In the HM domain, however, the specific branch length of scCO_2 increases to 1.62 by channelizing CO_2 flow induced by the heterogeneously distributed intermediate-wet patches (Chang et al. 2020). In this case, both of the specific branch and junction numbers, as well as the cluster numbers, are smaller than that of hexane. As the heterogeneously distributed OTS-altered patches became more wetting to the invading fluid, i.e., hexane, the flow channelization was weakened. In the UM domain, both scCO_2 and hexane develop similar specific branch length, whereas scCO_2 flow paths are more interconnected, inducing larger specific branch and junction number and smaller cluster number. The bridging flow topology of scCO_2 is in contrast with the fragmented flow characteristics of hexane (see Figures 5(f) and (i)).

Wetting state

Figure 5. The pore-scale flow characteristics of hexane, $scCO_2$ and mixed-wet effects through a topological skeleton analysis over a local pore domain (3.8 × 3.7 mm^2). (a) Pore geometry of the originally EW (WW) domain, with full-depth (40 μm) pores shown in yellow and half-depth (20 μm) pore throats in red (these color indicators are also applied to (b) through (i)). (b) and (c) show the mixed-wet patterns in the HM and UM domains, with unaltered pore space shown in yellow and altered pore space in white. (d), (e), (f) and (g), (h), (i) compare the quasi-steady state hexane and $scCO_2$ (in white) distribution in the EW(WW), HM and UM domains, respectively. The blue arrow represents the bulk flow direction in the micromodel, while the red dotted arrows indicate the hexane and $scCO_2$ flow directions within the local domain. The red solid arrows in (f) point to the snap-off of the non-wetting EG ganglions, while the blue solid arrow to the pore refilled by EG ganglion, which migrates from outside of the pore domain, over a length of tens of pore size after hexane breakthrough (see more details in Figure S5 of SI). The blue curve in (d), shown as an example, marks the individual hexane cluster isolated from others. (j) and (k) are the hexane and $scCO_2$ saturation distributions vs. pore/pore throat size within the pore domain quantified by the Local Thickness plugin in ImageJ software. The colored dash lines in the figures indicate the median of hexane/$scCO_2$ saturation distribution and corresponding pore/pore throat sizes in the three domains. (a), (b), (c) and (g), (h), (i) were modified from Chang et al. (2020).

Table 1. Distribution characteristics of hexane/$scCO_2$ flow paths

Wetting type	Cluster number	Specific branch number	Specific junction number	Specific branch length
EW (WW)	3/4	0.37/0.48	0.31/0.42	0.92/0.94
HM	10/6	0.49/0.22	0.40/0.18	0.93/1.62
UM	16/7	0.65/0.79	0.53/0.69	0.75/0.81

Note: The branch and junction number, and the average branch length were first calculated for hexane flow paths ($N_{b,hexane}$, $N_{j,hexane}$, and L_{hexane}) and for the pore domain (N_b, N_j and L), then their ratios were calculated and defined as the specific branch number ($N_{b,hexane}/N_b$), specific junction number ($N_{j,hexane}/N_j$) and specific branch length (L_{hexane}/L) for hexane. The same definition applies to $scCO_2$ and the corresponding values were presented after each hexane value in the table.

3.3.3 Pore-network-scale distribution characteristics

We have investigated the pore-scale flow characteristics of hexane and $scCO_2$ in a local pore domain. We further quantify the displacement and fragmented hexane invasion by applying the topological analysis to the three types of micromodels. Figure 6 compares the cluster number, specific branch number and specific branch length between hexane and $scCO_2$ for all experiments at imposed $logCa$ from −8.1 to −3.9. The variations of specific branch number vs. $logCa$, as shown in Figure S6 of SI are consistent with the specific junction number, which results from the development of new flow paths being accompanied by new junctions/interconnections. In Figures 6 (a), (b) and (c), both hexane and $scCO_2$ present similar flow characteristics at imposed $logCa$ values in the EW/WW micromodel, as expected given their identical pore geometries and similar viscosity ratios, IFTs, and contact angles between hexane-EG and $scCO_2$-brine.

In the HM micromodel, Figure 6(d) presents larger cluster numbers for hexane at large $logCa > -6.0$. The increase of cluster number for hexane is more pronounced in the UM micromodel for all imposed $logCa$ values (Figure 6(g)), indicating considerably fragmented distributions of hexane and well-mixed hexane and EG upon its displacement through the pore network composed of more uniformly distributed EG-wet or hexane-wet surfaces. The dispersed and fragmented hexane distributions result in larger specific branch number and smaller specific branch length in the HM and UM micromodels, when compared to those for $scCO_2$ (see Figures 6(e), (h) and (f), (i)). The flow characteristics of hexane and $scCO_2$ at the pore-network scale are consistent with the pore-scale observations presented in Section 3.3.2 and Table 1. Also note that the most pronounced differences between hexane-EG and $scCO_2$-brine distributions are for the specific branch length in the HM (Figure 6(f)) and the cluster number in the UM micromodels (Figure 6(g)), representing (1) channelized $scCO_2$ flow in former featured by most heterogeneously distributed intermediate-wet patches, and (2) dispersed hexane flow in the latter featured by largest wettability contrasts. Thus, specific branch length and cluster number may be able to better quantify the fingering flow regimes and mixed-wettability impacts.

The pore-network scale analysis of hexane and $scCO_2$ distributions indicates dispersed and fragmented invasion induced by displacement in strongly mixed-wet systems. In a GCS reservoir that presents mixed-wet rock surface, this implies decrease of drainage efficiency and CO_2 relative permeability (thus injectivity) during injection, but better mixing of CO_2 with resident brine, thus increase of CO_2 residual and dissolution trapping after injection ceases.

Figure 6. The cluster number, specific branch number, and specific branch length vs. $logCa$ for hexane and $scCO_2$ in the EW(WW), HM and UM micromodel.

3.4 $\log(dCa¿¿¿)-\log(iCa¿¿¿)¿¿$ diagram

The quasi-steady hexane saturations in the three types of micromodels show increased $logCa$ values at the saturation minima (corresponding to flow regime crossover) from −6.9 in the EW to −5.6 in both of the HM and UM micromodels. By comparison, the $logCa$ values corresponding to the minimum $scCO_2$ saturation are about constant. These indicate that $logCa$ is insufficient to quantify the drainage and imbibition flow, as the form of the capillary number in this presentation does not include any contact angle terms that describe the solid surface wettability. Lenormand et al. (1988) introduced the modified capillary number ($Ca^{¿}$) that considers the solid surface wettability, measured geometrically from the angle formed by a resident liquid at the three-phase boundary where a liquid, gas or another immiscible liquid, and solid intersect. The CO_2 saturation vs. $Ca^{¿}$ has been investigated by Chang et al. (2020) in the two mixed-wet systems where contact angles vary within 90° for $scCO_2$-brine. The single $Ca^{¿}$ was capable to describe the fingering and crossover flow regimes since drainage of brine is the dominant flow characteristics and no imbibition capillary number can be determined. In a mixed-wet system where contact angles vary beyond 90°, the capillary number needs to reflect the distribution of hydrophilic and hydrophobic pores because of their fundamentally different flow characteristics. Here, we introduce and define $dCa^{¿}$ and $iCa^{¿}$, where (1) $dCa^{¿}$ is the drainage capillary number determined by the cosine of the contact angle in the untreated patches wetting to resident fluid, thus for hexane-EG, $\theta_{r,1} = ¿47°$; and (2) $iCa^{¿}$ describes the imbibition capillary number, including the cosine of the contact angle in the treated patches wetting to invading fluid, thus for hexane-EG, $\theta_{r,2} = ¿145°$. $dCa^{¿}$ and $iCa^{¿}$ then can be calculated as follows:

$$dCa^{¿} = (\mu \times \bar{u}) / (\sigma \times c\,os' \theta_{r,1}) \quad \text{Eq. (1)}$$

$$iCa^{¿} = (\mu \times \bar{u}) / ¿¿ \quad \text{Eq. (2)}$$

where $\cos' \theta_r$ is derived from the pore space areas for EG-wet and hexane-wet patches (A_1 and A_2, respectively)

$$\cos' \theta_{r,1} = \frac{A_1 \cos \theta_{r,1}}{A_1 + A_2} \quad \text{Eq. (3)}$$

$$\cos' \theta_{r,2} = \frac{A_2 \cos \theta_{r,2}}{A_1 + A_2} \quad \text{Eq. (4)}$$

For the HM micromodel, $A_1 = A_2 = 0.50$; for the UM micromodel, $A_1 / (A_1 + A_2) = 0.30$; $A_2 / (A_1 + A_2) = 0.70$. These area-weighted presentations of capillary numbers are similar to Chang et al. (2020). Figure 7 presents the log $(d\,Ca^{¿})$ − log $(iCa¿¿¿)¿$ relations for the hexane injection tests in the two mixed-wet micromodels (marked by the diagonally ordered red dots). For the untreated EG-wet micromodel, $\cos' \theta_{r,1} = \cos \theta_{r,1} = \cos 47°$. It is noted that both drainage and imbibition present similar viscous fingering flow at high injection rates when capillary force is suppressed by strong viscous force, resulting in similarly high displacement efficiency. In the EG-wet systems, A_2 and $\cos' \theta_{r,2} = ¿\ 0$, therefore $iCa^{¿}$ in principle becomes infinitely large. In this case, we plotted tests in the

EG-wet micromodel at the $\log(iCa^{¿})$ averaged over the largest experimental $\log(dCa¿¿¿)¿$ values for EW (−3.7), HM (−3.5) and UM (−3.6) micromodels, representing the condition that both capillary drainage and imbibition are suppressed by strong viscous force and converge at $\log(iCa^{¿})$ = $\log(dCa¿¿¿)¿$ = −3.6. Decreasing either $\log(dCa¿¿¿)¿$ or $\log(iCa¿¿¿)¿$ induces more dominant drainage or imbibition flow by capillary force. The color map represents hexane saturation distribution vs. $\log(dCa¿¿¿)-\log(iCa¿¿¿)¿¿$determined by interpolating the 30 experimental results. Individual experiments are mapped on this plot as red dots labeled according to their micromodel abbreviations (EW, HM, and UM) and numbers from 1 to 10 to denote the specific experiment shown in Figure 3, where a larger number represents an experiment under higher hexane injection rate. The hexane saturation varies from 0.3 to 0.7 as indicated by the color bar (warmer color represents higher hexane saturation).

From the figure, we may conclude (1) high hexane saturations at both high or low $\log(dCa¿¿¿)¿$ and $\log(i\,Ca^{¿})$ values characterizing dominant viscous fingering or capillary fingering flow; (2) low hexane saturations at flow regimes transition, which occurs equivalently away from the strong viscous fingering 'corner' at the figure top right (bounded by the white dotted lines in Figure 7). At the fingering regime crossover, the minimum hexane saturation presents at $\log(dCa¿¿¿)=\log(i\,Ca^{¿})¿$=~−5.0, considering both solid surface wettability and area fractions of each wetting type. Also note that as the pore space is altered wetting to the invading fluid, the displacement efficiency (here hexane saturation) increases with decreasing $\log(i\,Ca^{¿})$ in the capillary fingering regime (marked by the white arrow at the bottom portion of Figure 7), which is a favorable trend for GCS, enhanced oil recovery, and non-aqueous phase liquid (NAPL) contamination/remediation, as subsurface flow is typically slow and flow is dominated by capillary force. The displacement efficiency, however, increases with increasing $\log(i\,Ca^{¿})$ in the viscous fingering regime (marked by the white arrow at the top portion of Figure 7), associated with fast subsurface flow present in the vicinity of injection wells.

While extensive lab and modeling studies have applied the classic $logM$- $\log Ca^{¿}$ diagram to quantify two-phase fingering flow after Lenormand (1988), we emphasize through Figure 7 the necessity to consider both $dCa^{¿}$ for drainage and $iCa^{¿}$ for imbibition to better characterize the fingering flow in a mixed-wet porous media where contact angles spatially vary beyond 90°. The figure could be improved through hexane injection tests in the same pore network OTS-treated to become uniformly wetting to hexane. Castro et al. (2015) reported water imbibition experiments in an initially oil-saturated and uniform water-wet micromodel. They observed non-monotonic variation of residual oil saturation as a function of (imbibition) capillary number, and presented highest residual oil saturations (thus lowest displacement efficiency) at $\log(i\,Ca^{¿})$=~−5.4, which is consistent with the crossover zone mapped in Figure 7. Considering impacts from of viscosities among fluid pairs, a three-dimensional $logM-\ \log(dCa¿¿¿)¿\ -\log(i\,Ca^{¿})$ diagram may be able to better predict the two-phase fingering flow characteristics in a strong mixed-wet porous media.

It should be noted that the two capillary numbers, $dCa^{¿}$ and $iCa^{¿}$, are based on average velocities and by area-weighted wettabilities within centimeter-scale pore networks. It remains to be determined how flow characteristics change as a function of mixed-wet patterns and area fractions of wetting patches. A better understanding of these requires hexane injections tests in more mixed-wet micromodels. It is also noted the 2-D nature of micromodels and their limitations in predicting two-phase flow in 3-D porous media. AlRatrout et al. (2018) quantified the contact angle distributions in mixed-wet rock samples using micrometer-resolution X-ray CT, and examined oil/brine displacement characteristics in 3-D. Similar to this study, they presented a wide range of local contact angles both above and below 90°, which facilitated the flow of both phases and increased displacement efficiency relative to the uniform water-wet and oil-wet samples. Rücker et al. (2018) imaged the pore-scale ganglion dynamics in a carbonate sample with fast synchrotron-based X-ray CT. They observed the mixed-wet pore space was intermittently filled with oil and brine ganglions. The frequency and size of these fluctuations were reported greater than in water-wet rock such that their impact on the overall flow and relative permeability cannot be neglected in modeling approaches. Note the similar flow of EG ganglions along with displacing hexane behind the invasion front, and refill of the pores preferentially invaded by hexane in Figure 5(f). While these fundamentals were observed in both 2-D micromodels and 3-D rock samples, we expect more considerable impacts from 3-D pore geometry and wettability heterogeneity. In addition, implications of these pore-scale laboratory results for field-scale reservoir behavior should be better understood with consideration of larger scale heterogeneity and gravity impacts.

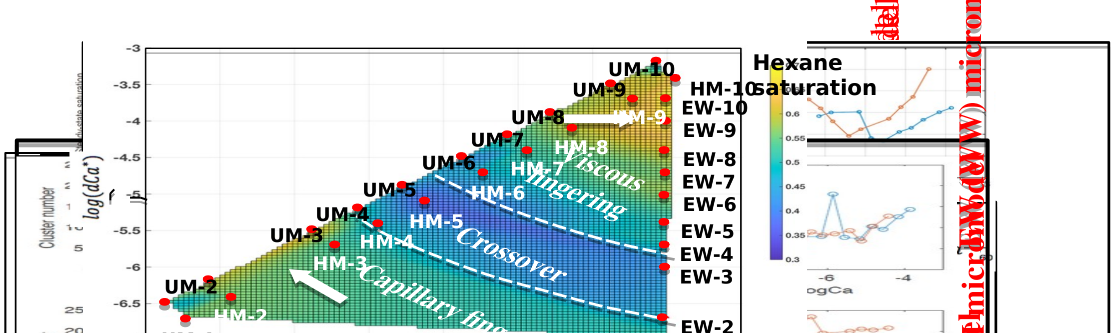

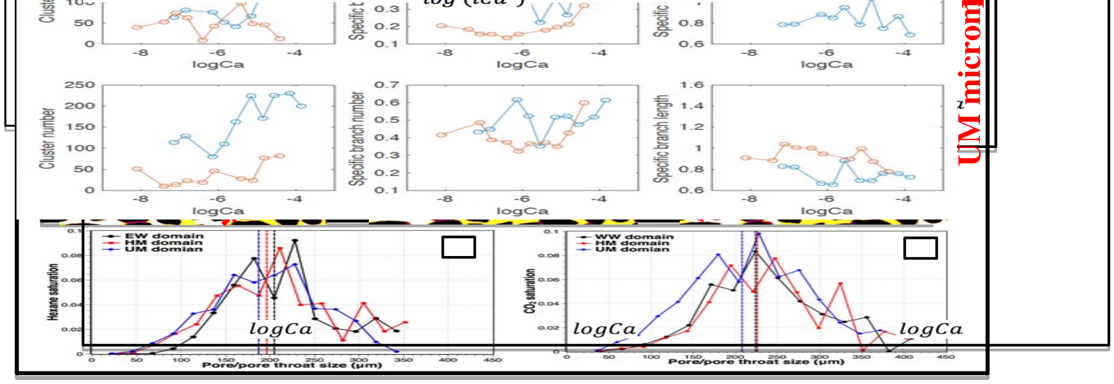

Figure 7. The log(*dCa*¿¿¿)−log (*iCa*¿¿¿)¿¿ relations for hexane injection tests in the EW-wet and two mixed-wet micromodels (marked by the red dots), and the steady-state hexane saturation distribution interpolated at the end of experiments. The white dotted lines bound the fingering flow regimes and crossover, while the white arrows point to the increasing tendency of hexane saturation. The label next to each red dot denotes an experiment in Figure 3, by combining the micromodel type (EW, HM and UM) with a number from 1 to 10, where a larger number represents an experiment under a higher hexane injection rate.

3.5 Pore-scale wettability distribution impacts on displacement

Large uncertainties in model predictions of multiphase flow in mixed-wet porous media have been recognized, indicating that the descriptor "mixed-wet" encompasses a wide range of displacement phenomena. For instance, Valvatne and Blunt (2004) conducted pore-scale modeling of oil-water displacement in mixed-wet sandstone rocks, and concluded that wettability characterization for mixed-wet systems imparts the greatest uncertainty to calculations. They suggested that reliable predictions require information on spatial correlations of mixed-wet patterns in order to ensure that the modeled relative permeability was in better agreement with experimental data. Modeling results from Zhao et al. (2010) further emphasizes the oil-wet fraction, which played a more important role in determining displacement efficiency than the contact angle in the oil-wet regions.

Pore network scale measurements needed to better relate mixed wettability and displacement efficiency are recently emerging. Alhammadi et al. (2017) use micro-CT for characterizing distributions of wettability within pore networks of a carbonate core. Akai et al. (2019) modeled oil-water flow in mixed-wet carbonate with different contact angle (water-wet, neutral-wet and oil-wet) assignments based on the measurements from Alhammadi et al. (2017). They concluded that inclusion of spatially heterogeneous wettability state is needed to correctly predict fluid conductivity in mixed-wet rocks. A recent modeling study by Foroughi et al. (2020) showed poor predictions of lab experiments in mixed-wet rock samples using randomly assigned distributions of contact angle. Improved predictions resulted when a mild degree of correlation between pore size and contact angle was included, with larger pores and throats tending to be more oil-wet. These modeling results suggested the importance of mixed-wettability patterns and their origins have consequences for the two-phase flow characteristics.

In our laboratory investigation, the wettability characteristics in the two mixed-wet systems were inherited from the pore-size distribution of the micromodels and flow distributions of coating agents used to establish different wettability patterns. Directly observed flow fundamentals of two different fluid pairs (hexane-EG and $scCO_2$-brine) through these pore networks with well-defined wettability distributions can help test and improve models. Better model predictions of reservoir behavior can be expected with further work on wettability distributions and correlations in pore networks in both micromodels and cores, combined with displacement experiments using different fluid pairs.

4. Conclusions

We created two mixed-wet micromodel systems that present uniformly and heterogeneously distributed patches strongly wetting to the invading hexane. These mixed-wet systems were tested to compare with hexane invasion into the unaltered pore space strongly wetting to the resident EG. Hexane-EG displacements were investigated and compared with $scCO_2$-brine displacements performed in the same micromodels. Along with the control tests in originally EG/water-wet micromodel, we observe similar displacement efficiency and distribution characteristics of hexane/$scCO_2$ in the untreated micromodel, due to the similar viscosity ratios and IFT between hexane-EG and $scCO_2$-brine. Compared to the untreated EG-wet micromodel, we show in the two mixed-wet micromodels overall increase of hexane saturation at the capillary fingering regime, and decrease of the value at the viscous fingering regime. The displacements for hexane-EG were in contrast with the dominant drainage flow for $scCO_2$-brine in the same mixed-wet micromodels, revealing more dispersed and fragmented invading fluid distribution and lower displacement efficiency in the former. We present a new set of capillary numbers, dCa¿describing drainage and $i\,Ca$¿ describing imbibition, to characterize the displacement efficiency and fingering flow regimes in the mixed-wet systems. Laboratory results indicate that a large wettability contrast may reduce $scCO_2$ storage efficiency during injection. However, the fluid phase distribution characteristics induced during immiscible fluid displacement through mixed-wet systems may enhance subsequent CO_2 residual and dissolution trapping after injection ceased.

The combined results from this study and our previous work (Chang et al., 2020), as well as from other cited recent studies on wettability distributions suggest that the effects of 'mixed-wet' reservoir conditions on multiphase displacement are more complicated than we previously thought. The observations help to understand the complexities and modeling uncertainties. The ranges of contact angle variation ('weak' and 'strong' mixed-wet systems), and resulting transitions of displacement characteristics from drainage dominant to co-occurring drainage and imbibition, should be taken into consideration. In addition to GCS, results from this study may also apply to other subsurface and reservoir processes including oil recovery and remediation of hydrocarbon-contaminated aquifers, where a more viscous resident fluid is displaced by a lower viscosity invading fluid and reservoir rocks present mixed-wet surfaces.

Supporting Information (SI)

More detailed information on the contact angle measurements, migrations of individual EG ganglions and characterizations on the flow regimes are provided in the SI.

Conflicts of interest

The authors declare no competing financial interest.

Acknowledgements

This material was based upon the work supported by the U.S. Department of Energy, Office of Science, Office of Basic Energy Sciences, Energy Frontier Research Centers program under Contract no. DE-AC02-05CH11231. We appreciate the valuable comments provided by the reviewers and the Associate Editor, which helped improve presentation of this work. Data are deposited in the Dryad repository with DOI: 10.7941/D1XK99, and available through the following link: https://datadryad.org/stash/share/aE0RA5mc1wd2z1u_CS2sx17-AgN9FaWKBKA03UTBZ68.

References

Akai, T., Alhammadi, A. M., Blunt, M. J., & Bijeljic, B. (2019). Modeling oil recovery in mixed-wet rocks: Pore-scale comparison between experiment and simulation. Transp. Porous Med., 127(2), 393–414.

Al-Khdheeawi, E., Vialle, S., Sarmadivaleh, M., Barifcani, A., & Iglauer, S. (2017). Impact of reservoir wettability and heterogeneity on CO_2 plume migration and trapping capacity. *Int. J. Greenhouse Gas Control*, 58, 142–158.

Alhammadi, A. M., AlRatrout, A., Singh, K., Bijeljic, B., & Blunt, M. J. (2017). In situ characterization of mixed-wettability in a reservoir rock at subsurface conditions. *Sci. Rep.*, 7(1), 10753.

AlRatrout, A., Blunt, M. J., & Bijeljic, B. (2018). Wettability in complex porous materials, the mixed-wet state, and its relationship to surface roughness. *Proc. Natl. Acad. Sci. U.S.A.*, 115(36), 8901–8906.

Anderson, W.G. (1986). Wettability literature survey — part 1: rock/oil/brine interactions and the effects of core handling on wettability. *J. Petrol. Technol.,* 38, 1125−1144.

Anderson, W. G. (1987a). Wettability literature survey — part 4: effects of wettability on capillary pressure. *J. Petrol. Technol.* 39 (10), 1283–1300.

Anderson, W.G. (1987b). Wettability literature survey — part 6: the effects of wettability on water flooding. J. Petrol. Technol. 39 (12), 1605–1622.

Arganda-Carreras, I., Fernandez-Gonzalez, R., Munoz-Barrutia, A., & Ortiz-De-Solorzano, C. (2010). 3D reconstruction of histological sections: Application to mammary gland tissue. *Microsc. Res. Tech.*, 73 (11), 1019–1029.

Armstrong, R. T., & Steffen, B. (2013). Interfacial velocities and capillary pressure gradients during Haines jumps. *Phys. Rev. E*, 88(4), 600–614.

Armstrong, R. T., Georgiadis, A. Ott, H. Klemin, D., & Berg, S. (2014). Critical capillary number: Desaturation studied with fast X-ray computed microtomography, *Geophys. Res. Lett.*, 41, 55–60, doi:10.1002/2013GL058075.

Castro, A. R., Shokri, N., Karadimitriou, N., Oostrom, M., & Joekar-Niasar, V. (2015). Experimental study on nonmonotonicity of Capillary Desaturation Curves in a 2-D pore network. *Water Resour. Res.*, 51, 8517–8528.

Chang, C., Kneafsey, T. J., Zhou, Q., Oostrom, M., & Ju, Y. (2019a). Scaling the impacts of pore-scale characteristics on unstable supercritical CO_2-water drainage using a complete capillary number. *Int. J. Greenhouse Gas Control*, 86, 11–21.

Chang, C., Zhou, Q., Kneafsey, T. J., Oostrom, M., & Ju, Y. (2019b). Coupled supercritical CO_2 dissolution and water flow in pore-scale micromodels. *Adv. Water Resour.*, 123, 54–69.

Chang, C., Kneafsey, T. J., Wan, J., Tokunaga, T. K., & Nakagawa, S. (2020). Impacts of mixed-wettability on brine drainage and supercritical CO_2 storage efficiency in a 2.5-D heterogeneous micromodel. *Water Resour. Res.*, 55, e2019WR026789. https://doi.org/10.1029/2019WR026789.

Cihan, A., Birkholzer, J., Illangasekare, T. H., & Zhou, Q. (2014). Amodeling approach to represent hysteresis in capillary pressure-saturation relationship based on fluid connectivity in void space. *Water Resour. Res.*, 50, 119–131, doi:10.1002/2013WR014280.

Cottin, C., Bodiguel, H., & Colin, A. (2011). Influence of wetting conditions on drainage in porous media: A microfluidic study. *Phys. Rev. E*, 84(2), 026311.

Dong, M., & Chatzis, I. (1995). The imbibition and flow of a wetting liquid along the corners of a square capillary tube. *J. Colloid Interface Sci.*, 172, 278−288.

Ferer, M., Ji, C., Bromhal, G. S., Cook, J., Ahmadi, G., & Smith, D. H. (2004). Crossover from capillary fingering to viscous fingering for immiscible unstable flow: Experiment and modeling. *Phys. Rev. E*, 70 (1), 016303.

Foroughi, S., Bijeljic, B., Lin, Q., Raeini, A. Q., & Blunt M. J. (2020). Pore-by-pore modeling, analysis, and prediction of two-phase flow in mixed-wet rocks. Phys. Rev. E, 102, 023302, 10.1103/PhysRevE.102.023302.

Gribanova, E., Molchanova, L., Grigorov, O., & Porova, V. pH dependence of contact angles on glass and quartz. *Colloid J. USSR*, 1976, 38, 504−506.

Hildebrand, T., & Rüesgsegger, P. (1996). A new method for the model-independent assessment of thickness in three-dimensional images. *J of Microscopy*, 185, 67−75.

Hilfer, R., & Øren, P. E. (1996). Dimensional analysis of pore scale and field scale immiscible displacement. *Transp. Porous Med*., 22, 53–72.

Hirasaki, G. J. (1991). Wettability: Fundamentals and Surface Forces. *SPE J.*, 6(02), 217-226.

Hu, R., Wan, J., Kim, Y., & Tokunaga, T. K. (2017a). Wettability effects on supercritical CO_2-brine immiscible displacement during drainage: Pore-scale observation and 3D simulation, Int. J. Greenhouse Gas Control, 60, 129–139.

Hu, R., Wan, J., Kim, Y., & Tokunaga, T. K. (2017b). Wettability impact on supercritical CO2 capillary trapping: Pore-scale visualization and quantification, *Water Resour. Res.*, 53, 6377–6394, doi:10.1002/2017WR020721.

Hughes, R. G., & Blunt, M. J. (2000). Pore Scale Modeling of Rate Effects in Imbibition. *Transp. Porous Med.*, 40, 295–322.

Iglauer, S. (2017). CO_2–Water–Rock Wettability: Variability, Influencing Factors, and Implications for CO_2 Geostorage. *Acc. Chem. Res.*, 50, 5, 1134–1142.

Jadhunandan, P. P., & Morrow, N. R. (1995). Effect of Wettability on Waterflood Recovery for Crude-Oil/Brine/Rock Systems, *SPE J.*, 10(1), 40–46.

Kang, Q., Zhang D., & Chen, S. (2004). Immiscible displacement in a channel: simulations of fingering in two dimensions. *Adv. Water Rescour.*, 27(1), 13–22.

Kumar, M., Fogden, A., Senden, T., & Knackstedt, M. (2012). Investigation of pore-scale mixed wettability, *SPE J.*, 17(1), 20–30.

Kuo, C.W., & Benson, S. (2015). Numerical and analytical study of effects of small scale heterogeneity on CO_2/brine multiphase flow system in horizontal corefloods. *Adv. Water Resour.*, 79, 1–17.

Lenormand, R., Touboul, E., & Zarcone, C. (1988). Numerical models and experiments on immiscible displacements in porous media. *J. Fluid Mech.*, 189, 165–187.

Levine, J. S., Goldberg, D. S., Lackner, K. S., Matter, J. M., Supp, M. G., & Ramakrishnan, T. S. (2014). Relative permeability experiments of carbon dioxide displacing brine and their implications for carbon sequestration, *Environ. Sci. Technol.*, 48(1), 811–818.

Morrow, N. R., Lim, H. T., & Ward, J. S. (1986). Effect of Crude-Oil-Induced Wettability Changes on Oil Recovery, *SPE J.*, 1(01), 89-103.

Morrow, N. R. (1990). Wettability and its effect on oil recovery. *J. Petrol. Technol.*, 42 (12), 1476–1484.

Nicolaides, C., Jha, B., Cueto-Felgueroso, L., & Juanes, R. (2015). Impact of viscous fingering and permeability heterogeneity on fluid mixing in porous media. *Water Resour. Res.*, 51, 2634–2647, doi:10.1002/2014WR015811.

Nittmann, J., Daccord, G., & Stanley, H. E. (1985). Fractal growth of viscous fingers: quantitative characterization of a fluid instability phenomenon. *Nature*, 314(14), 141–144.

Nguyen, V. H., Sheppard, A. P., Knackstedt, M. A., & Pinczewski, W. V. (2006). The effect of displacement rate on imbibition relative permeability and residual saturation. *J. Petrol. Sci. Eng.*, 52(1-4), 54–70.

Rasband, W. S. (1997–2021). ImageJ, U.S. National Institutes of Health, Bethesda, Maryland, USA, https://imagej.nih.gov/ij/.

Roof, J. (1970). Snap-off of oil droplets in water-wet pores, *SPE J.*, 10, 85–91.

Rücker, M., Bartels, W. B., Singh, K., Brussee, N., Coorn, A., van der Linde, H., Bonnin, A., Ott, H., Hassanizadeh, S. M., Blunt, M. J., Mahani, H. Georgiadis1, A., & Berg, S. (2019). The effect of mixed wettability on pore-scale flow regimes based on a flooding experiment in Ketton limestone. Geophys. Res. Lett., 46, 3225–3234.

Saffman, P. G., & Taylor, G. (1958). The penetration of a fluid into a porous medium or Hele-Shaw cell containing a more viscous liquid. *Proc. R. Soc. A*, 245, 312–329.

Sahimi, M. (1993). Flow phenomena in rocks—from continuum models to fractals, percolation, cellular automata, and simulated annealing. *Rev. Mod. Phys.*, 65 (4), 1393–1534.

Salathiel, R. A. (1973). Oil recovery by surface film drainage in mixed-wettability rocks. *J. Petrol. Technol.*, 25, 1216–1224.

Tokunaga, T. K. (2009), Hydraulic properties of adsorbed water films in unsaturated porous media, Water Resour. Res., 45, W06415, doi:10.1029/2009WR007734

Tokunaga, T. K. (2009), Hydraulic properties of adsorbed water films in unsaturated porous media, Water Resour. Res., 45, W06415, doi:10.1029/2009WR007734

Tokunaga, T. K. (2009). Hydraulic properties of adsorbed water films in unsaturated porous media, *Water Resour. Res.*, 45, W06415, doi:10.1029/2009WR007734.

Valvatne, P. H., & Blunt, M. J. (2004). Predictive pore-scale modeling of two-phase flow in mixed wet media, *Water Resour. Res.*, 40, W07406, doi:10.1029/2003WR002627.

Wang, Y., Zhang, C., Wei, N., Oostrom, M., Wietsma, T. W., Li, X., & Bonneville, A. (2012). Experimental study of crossover from capillary to viscous fingering for supercritical CO_2–water displacement in a homogeneous pore network. *Environ. Sci. Technol.*, 47, 212–218.

Xu, B., Yortsos, Y. C., & Salin, D. (1998). Invasion percolation with viscous forces. *Phys. Rev. E*, 57, 739–751.

Zhang, C., Oostrom, M., Wietsma, T. W., Grate, J. W., & Warner, M. G. (2011). Influence of Viscous and Capillary Forces on Immiscible Fluid Displacement: Pore-Scale Experimental Study in a Water-Wet Micromodel Demonstrating Viscous and Capillary Fingering. *Energ. Fuels*, 25 (8), 3493–3505.

Zhao, B., MacMinn, C. W., & Juanes, R. (2016). Wettability control on multiphase flow in patterned microfluidics. *Proc. Natl. Acad. Sci. U.S.A.*, 113 (37), 10251–10256.

Zhao, X., Blunt, M.J., & Yao, J. (2010). Pore-scale modeling: effects of wettability on waterflood oil recovery. J. Petrol. Sci. Eng., 71, 169–178.